Lawrence Berkeley National Laboratory

Title
Flow simulation and analysis of high-power flow batteries

Permalink

Authors
Knudsen, E
Albertus, P
Cho, KT
et al.

Publication Date

DOI

Peer reviewed

High-Power Flow Batteries, Part II: Flow Field Modeling And Simulation

E. Knudsen[a,*], P. Albertus[a], K. T. Cho[c], A. Weber[b], A. Kojic[a]

[a]*Bosch Research and Technology Center, 4005 Miranda, Palo Alto CA 94304*
[b]*Lawrence Berkeley National Laboratory, 1 Cyclotron Road, Berkeley CA 94720*
[c]*Northern Illinois University, Dept. of Mechanical Engineering, Dekalb, IL 60115*

Abstract

Cost concerns have played an important role in limiting the deployment of flow battery technology. A possible method of lowering flow battery costs is to increase power density and thereby reduce stack area. If per-pass utilizations are held constant, increasing a battery's power density requires higher flow rates. In this second of a two-paper series we present a 3D computational fluid dynamics model of a flow battery flow field and porous electrode with the flow rates required for higher power densities. Both interdigitated and serpentine designs, and cell sizes of between 10 cm^2 and 400 cm^2, are simulated. Results include the scaling of pressure losses with flow rate and design parameters, relative fluid flux through the porous and open channel flowpaths, and the key timescales associated with convection and diffusion processes.

Keywords:

1. Introduction

As the share of global electricity generated by intermittent sources such as solar and wind grows, increasing attention is being placed on energy storage technologies that can handle grid-scale demand. Flow batteries [1, 2, 3] have been proposed as a means of addressing grid scale needs [4, 5, 6] because their capacity can be increased simply by using larger active material storage tanks. However, these batteries are subject to a number of materials and engineering challenges that tend to increase system costs and inhibit realizability [6]. Many of the cost challenges can be addressed by moving towards higher power density stacks, which reduce the area and hence material required for a given power output. In the first paper [7] of this two-paper set an analysis of the requirements for realizing high-power densities was presented. Particular focus was placed on design parameters such as flow rates, electrode thicknesses and pumping losses, and comparisons between state of the art and high-power designs were performed. That analysis provided a quantitative spectrum of the flow rates, electrode thicknesses, and other system parameters that would help to lower battery costs. This second paper considers the transport physics associated with the higher flow rates required for higher power densities.

Two flow transport processes particularly influence the performance of a flow battery cell. First, the pressure drop required to move reactants throughout the system directly affects cell efficiency. Minimizing this pressure drop will allow more of the cell's energy to be devoted to useful work. Second, the flow distribution within a flow plate and electrode has a direct impact on mass transport to the reaction sites on the surface of the porous electrodes. For example, if a flow dead zone occurs within a porous electrode then mass transport will be supported only by diffusion and migration. This can significantly reduce the local current density relative to other regions where reactants are being actively supplied through convection. The presence of flow dead zones can also lead to localized degradation because they can foster local electrochemical or chemical conditions that drive unwanted processes (e.g., carbon corrosion). Figure 1 shows an example of degradation in a 50 cm^2 variant of an experimental H_2/Br_2 flow cell [6, 8]. Similarly, neutron imaging has indicated [9] that transport limitations occur around complex flow features in fuel cell flow plates. The importance of reactant transport in flow batteries motivates the need for a detailed understanding of

---

*Corresponding author.
Email address: `ewk@alumni.stanford.edu` (E. Knudsen)
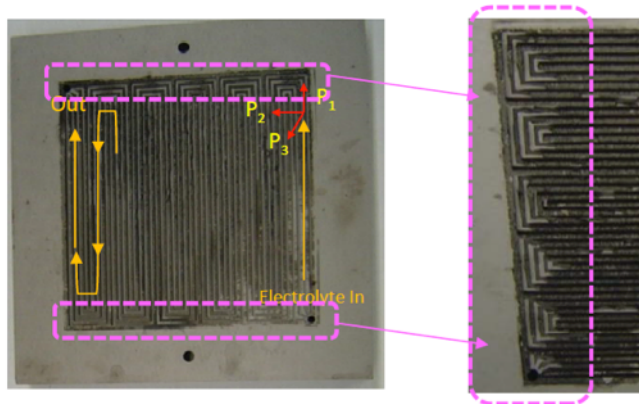
Figure 1: Example of flow plate degradation seen in a 50 cm^2 H$_2$/Br$_2$ serpentine flow battery cell operated at 6 mA/cm^2 for 100 hours between cutoff potentials of 1.25 V and 0.80 V. Degradation was more likely to be found around the bends of the flow channels.

convection within these cells. Here, three-dimensional (3D) computational fluid dynamics (CFD) tools are used to advance this understanding.

The application of CFD modeling to flow batteries is limited, but the technique has been used to study flow through many other electrochemical systems. Several studies have focused on Proton-Exchange Membrane Fuel Cells (PEMFCs), and have limited their investigation to isolated sections of a cell layer. For example, Um et $al.$ [10] developed a 2D CFD and electrochemical model of a hydrogen fuel cell using a representative layer consisting of parallel channels. Their model reproduced experimental cell voltage curves and described sensitivities to hydrogen concentrations in the anode gas stream. Berning and Djilali [11] developed a 3D CFD and electrochemical model of a PEMFC. Single anode, cathode, and water transport channels in one cell layer were computed and water phase change mechanisms were included in the model. The concentration of liquid water and the dynamics of phase change were investigated, and transport phenomena were noted to be strongly three dimensional. Lum and McGuirk [12] worked primarily with a 2D model of a PEMFC, but also considered 3D simulations. The domain of study was two channels from an interdigitated flow field design. 3D transport processes were found to be important, and the interdigitated design was found to provide better polarization behavior than a conventional gas distributor, where mass transfer limitations are observed at lower current densities. Schwarz and Djilali's [13] model of a 3D PEMFC similarly considered a single representative channel and employed a thin film agglomerate model to describe the catalyst layers. The model was used to investigate transport limitations and ohmic losses in the cell's catalyst layers. Additional single channel PEMFC models appear in the work of Ubong et $al.$ [14] and Darling and Badrinarayanan [15].

Researchers have also extended these models beyond individual channels in order to compute the behavior of full cell layers. For example, Yan et $al.$ [16] created 3D PEMFC models of 5 cm^2 cell layers with parallel, serpentine, and Z-type flow plate designs. Polarization curves were affected by the flow field design at higher current densities, and the pressure drops associated with the different designs were compared. Huang and Lin [17] considered a 3D PEMFC with a 3 channel serpentine flow field design and an active area of 25 cm^2. They used a Levenberg-Marquardt method to redesign the height of the channel sections near the flow plate outlet. Sinha et $al.$ [18] also modeled a 3 channel, serpentine, 25 cm^2 PEMFC. They performed both full cell and single channel calculations, and studied inlet humidity sensitivities and the effect of oxygen depletion. Kvesić et $al.$ [19] simulated a 5 cell PEMFC stack with individual cell areas of 200 cm^2. To promote computational tractability, their study invoked a lumped porous model in which the geometric details of the flow plates in each cell were not resolved. Instead, flow fields were treated as porous media layers in which the porosity spatially varied as a function of the flow field design. Liu et $al.$ [20] considered spiral flow field designs for PEMFC's, and compared them to serpentine flow field designs. They found that for active cell areas of around 10 cm^2, a spiral design provides better material transport through electrodes. They also noted that the flow field geometry has a significant effect on gas distribution in the cell. A comprehensive review of how flow field parameters influence PEMFC performance was performed by Manso et $al.$ [21].

2
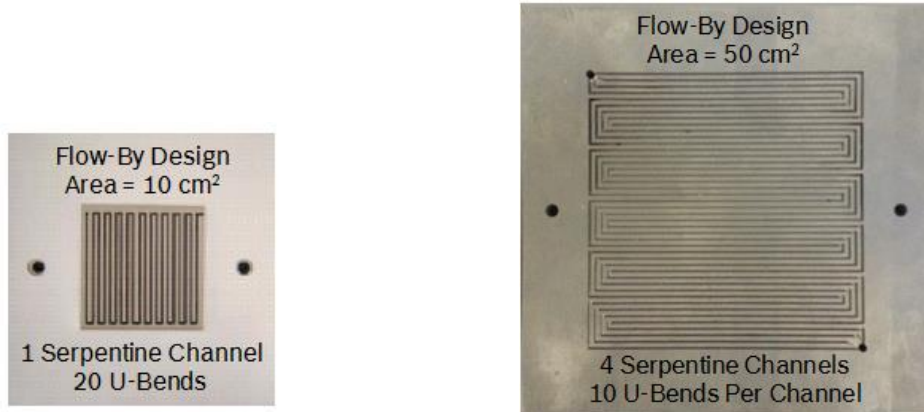
(a) 10 cm² single channel serpentine flow plate   (b) 50 cm² four channel serpentine flow plate

Figure 2: Examples of the serpentine flow pate hardware used in the flow battery experiments in [6, 8]. These graphite plates were manufactured by Fuel Cell Technologies, Inc.

Channel design, flow direction, channel length and number, channel cross section shapes, and baffle designs were all considered.

While some analysis from PEMFC literature is directly applicable to Vanadium / Vanadium [22], Hydrogen / Bromine [6, 8, 23], and other redox flow batteries, important differences between PEMFCs and flow batteries exist. These differences include the use of single phase transport in many flow battery half cells, and they motivate the consideration of designs specific to flow battery requirements. While less common, CFD models of flow battery systems have been developed by a few groups. Latha and Jayanti [24] analyzed flow battery hydrodynamics using both experimental and 3D CFD analyses. They compared pressure drops and velocities in representative sections of interdigitated and serpentine flow plate designs, and particularly noted why these designs might be viewed differently from fuel cell and from flow battery perspectives. Brunini *et al.* [25] developed a 3D single channel model of a novel semi-solid variety of flow battery [26] in which both electrically conductive and solid, ion accepting particles are suspended in a transported liquid medium. The model was used to investigate how voltage dependencies on state-of-charge influence the system's performance. This same group has also developed a 2D semi-solid flow battery CFD model [27].

In this paper the hydrodynamics of several flow battery cell designs are investigated to understand how transport processes affect battery operation. This paper builds upon previous work by considering the higher flow rates that are needed to achieve high power densities, by simulating complete flow fields with much larger active areas of up to 400 cm², and by performing more detailed analyses of mass flux splits between porous electrodes and open channels. This introduction serves as section 1 of the paper. Section 2 describes the different flow plate designs that are considered. The governing equations and computational infrastructure used for the CFD calculations are presented in section 3. Computational results are shown in section 4, and the paper's conclusions are reviewed in section 5.

2. Simulated cases

The H_2/Br_2 cell studied by Cho *et al.* [6, 8] is considered here. This system was experimentally tested using both 10 cm² flow-through and 10 cm² and 50 cm² flow-by serpentine flow plates. Representative flow plate hardware from these studies is shown in in Fig. 2. During operation, a porous electrode is placed on the face of these plates, so that an interface is formed between the open flow channels in the plates and the porous electrode layer. Reactant transport to active electrochemical sites in the electrode depends on the dynamics of the flow across this interface. Only the liquid (Br_2) side of the H_2/Br_2 cell will be simulated, since gaseous H_2 transport is expected to be less of a limiting factor than aqueous Bromine solution transport.

As discussed in the first paper [7] of this set, flow-through electrode designs can be used for flow batteries when low current densities are acceptable. In these flow-through designs, no channels are made in the battery flow plates and fluid travels across the entire area of the cell through the porous electrode. The flow

3

(a) 10 cm^2 serpentine, 1 channel   (b) 50 cm^2 serpentine, 4 channels

(c) 50 cm^2 loose interdigitated   (d) 50 cm^2 tight interdigitated   (e) 400 cm^2 loose interdigitated
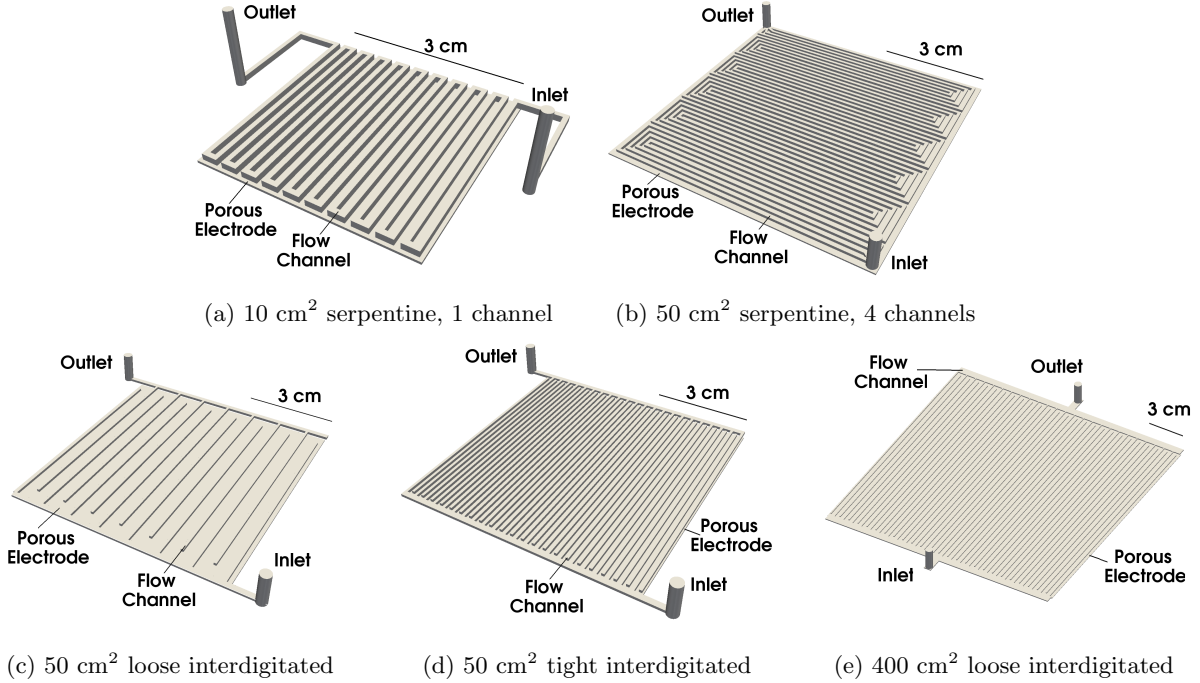
Figure 3: Simulated flow battery flow field designs. Inlet and outlet locations in the serpentine cases were chosen to match the hardware from Fig. 2. Inlets and outlets in the 50 cm^2 interdigitated cases were chosen to provide consistency with the 50 cm^2 serpentine design, while in the 400 cm^2 case a more symmetric inlet and outlet configuration was used by default.

rates required to support low current densities result in acceptable pressure drops. Flow-through designs are not appropriate for higher current densities, however, because higher flow rates are required. These higher flow rates can only be achieved in a flow through electrode with large pressure gradients that are driven by pumping systems which consume significant energy. This observation assumes that all flow in a flow-through design passes through an electrode of uniform porosity. More elaborate flow-through-like designs with spatially varying porosity have been proposed [28] and may result in acceptable pressure drops, but such designs are not considered here.

The goal of minimizing pressure losses while supplying sufficient reactants to the electrode forces the consideration of flow-by designs. In these designs, open channels are cut into a cell's flow plates. The open channels provide fluid with lower resistance paths across the cell area. For example, Darling and Perry [29] experimentally compared the performance of a flow-through Vanadium flow battery with that of two flow-by designs. They found that the flow-through design would lead to significantly larger pressure drops than the flow by designs as the cell size was scaled up toward industrial applicability. They also analyzed sensitivities to the transport phenomena that must be accounted for when switching between flow field designs.

Five flow-by designs that include three different cell sizes are simulated. Figure 3 depicts the selected flow field geometries. The first two are serpentine channel designs: one 10 cm^2 design utilizing a single channel (Fig. 3a), and one 50 cm^2 design utilizing four channels (Fig. 3b). The channel in the 10 cm^2 serpentine design consists of 20 long passages connected by bends. The cross section of this channel is 1.016 mm high and 0.7874 mm wide. The spacing between channels is 0.853 mm. The dimensions of the 10 cm^2 serpentine design were chosen to match the experimental flow plates used in [6] and [8], which were manufactured by Fuel Cell Technologies, Inc. The four channels in the 50 cm^2 serpentine design all consist of 11 long passages (44 in total) connected by bends. The cross section of each channel is the same, measuring 0.795 mm high and 0.795 mm wide. The spacing between channels is 0.795 mm.

The next three designs employ InterDigitated Flow Fields (IDFFs). The dimensions of the IDFF channels were chosen to provide some basic similarity with the serpentine hardware specifications. The first two IDFF

(a) 0.4 mm electrode   (b) 1.2 mm electrode   (c) 2.4 mm electrode
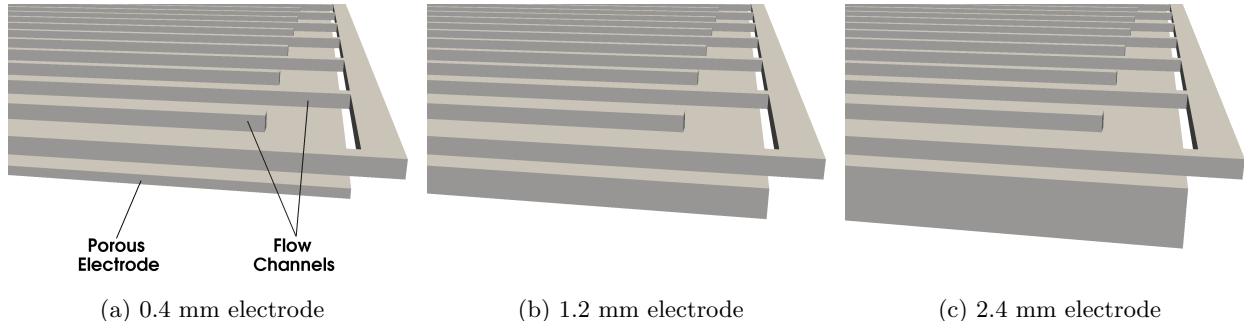
Figure 4: Comparison of electrode thicknesses, shown using the 50 cm^2 loose interdigitated flow field.

Flow Plate Design	Reynolds # In Channel
10 cm^2 serpentine	126
50 cm^2 serpentine	157
50 cm^2 loose idff	139
50 cm^2 tight idff	47
400 cm^2 loose idff	333

(a) 1 mL min^{-1} cm^{-2} flow rate

Flow Plate Design	Reynolds # In Channel
10 cm^2 serpentine	629
50 cm^2 serpentine	786
50 cm^2 loose idff	694
50 cm^2 tight idff	237
400 cm^2 loose idff	1667

(b) 5 mL min^{-1} cm^{-2} flow rate

Table 1: Estimated Reynolds numbers in the individual channels of each flow plate design.

designs both have active cell areas of 50 cm^2, but different spacings between channels. In the loosely spaced case (Fig. 3c), the distance between flow channels is 4.0 mm. This design has 15 channels in total, and each channel has a width and height of 0.8 mm. In the tightly spaced design (Fig. 3d), the distance between channels is 0.8 mm. This design's 44 channels also have widths and heights of 0.8 mm. The third IDFF geometry has a larger active cell area of 400 cm^2 (Fig. 3e). This cell area was considered in an effort to approach more industrially relevant cell sizes. The design is characterized by a relatively loose channel spacing of 3.2 mm. The 50 channels have widths and heights of 0.8 mm.

Three different electrode thicknesses are used in the simulations. As shown with a 50 cm^2 loose interdigitated flow plate in Fig. 4, these electrode thicknesses are 0.4 mm, 1.2 mm, and 2.4 mm. The last of these values is too thick to be considered for use in a practical device due to ohmic drops (see [7]). It is helpful, however, for exposing the electrode's influence on hydrodynamics.

The liquid half cell hydrodynamic systems are simulated using area specific flow rates of between 0.5 mL min^{-1} cm^{-2} and 30 mL min^{-1} cm^{-2}. These flow rates encompass the range of viable values that were discussed in part one [7] of this two-paper series. Water is used as the working fluid in all simulations to represent the aqueous Bromine solution that passes through one side of an H_2/Br_2 flow battery. Actual electrolyte fluids may have higher viscosities [29], which would further increase the pressure drops found in this analysis.

Representative Reynolds numbers describing flow through individual channels are shown in Table 1. This table assumes the total flow across each plate is equally distributed amongst the channels. For the serpentine designs, the table also assumes that 60% of the total flow passes through the open channels, with the remainder passing through the electrode (see Fig. 8 for more exact flux splits). For the interdigitated designs, the numbers assume that 100% of the flow passes through half of the total number of channels (the flow passes from the inlet channels to the outlet channels through the electrode). In reality, the velocities in the channels can deviate significantly from the values implied by Table 1, and the tabulated Reynolds numbers only provide baseline information.

Data from Gostick *et al.* [30] is the source of the carbon electrode material's permeability and porosity. The permeability of the electrode is set as $\kappa = $ 1E-11 m^2 and the porosity is set as $\gamma = 0.9$. To understand the influence of the electrode permeability, additional simulations are performed using values of $\kappa = $ 1E-

10 m^2 and $\kappa = $ 1E-9 m^2. This range is quite wide, but it clearly exposes trends and it encompasses the electrode permeabilities that were simulated in [24]. In a real cell, permeability is expected to depend on the compression applied to the porous electrode.

3. Simulation methodology

3.1. Governing equations

Flow in the electrodes and channels is solved with the steady, incompressible, Reynolds Averaged Navier-Stokes equations with porous media transport terms included,

$$\frac{\partial}{\partial x_j}\left(\gamma\overline{\rho u_j}\right) = 0, \tag{1}$$

$$\frac{\partial}{\partial x_j}\left(\gamma\overline{\rho u_i}\overline{u_j}\right) = -\gamma\frac{\partial}{\partial x_i}\left(\overline{p}\right) + \frac{\partial}{\partial x_j}\left(\gamma\left(\overline{\tau}_{ij}+\overline{\sigma}_{ij}\right)\right) - \frac{\overline{\rho}\nu}{\kappa}\overline{u_i}, \tag{2}$$

where u_j is the velocity in the jth direction, ρ is the density, p is the pressure, γ is the porosity, κ is the permeability, and ν is the kinematic viscosity. The overline symbol $(\overline{\cdot})$ denotes ensemble averaging. The porosity γ is constant in both the open channel region (γ=1) and the electrode region, so that its placement inside gradient operators is only relevant at the flow plate / electrode interface. The viscous stress tensor τ_{ij} and the Reynolds stress tensor, σ_{ij}, are,

$$\tau_{ij} = \overline{\rho}\nu\left[\left(\frac{\partial u_i}{\partial x_j}+\frac{\partial u_j}{\partial x_i}\right) - \frac{2}{3}\delta_{ij}\frac{\partial u_k}{\partial x_k}\right], \tag{3}$$

$$\sigma_{ij} = \overline{\rho u_i}\overline{u_j} - \overline{\rho u_i u_j}. \tag{4}$$

For the most part, the Reynolds numbers in the flow battery half cells are low and flow structures are laminar. No turbulence model is needed in such conditions. At high flow rates, however, velocities in open channel regions may become large enough to reach Reynolds numbers associated with transition or weak turbulence. The ensemble averaged form of the Navier-Stokes equations is solved to allow for this possibility. A realizable k-ϵ turbulence model [31, 32, 33] is used to close the Reynolds stress tensor σ_{ij} in this ensemble averaged framework. The use of this turbulence closure does influence the quantitative simulation results reported below.

3.2. Meshes

Meshes were created for each of the flow battery half cells in Fig. 3 using OpenFOAM's Snappy-HexMesh [34] tool. Cell counts from these meshes are shown in table 2. Rows with multiple entries in the third column indicate that mesh sensitivity was tested by running a single operating point using different mesh resolutions. For example, the 50 cm^2 serpentine mesh was simulated using mesh sizes ranging from 6.9 million cells to 20.2 million cells. The calculated pressure difference across the half cell changed by several percent as the mesh resolution was adjusted. This magnitude of variation is small in comparison to the pressure ranges that are presented in the results section below. At least 8 cells were placed across flow channels in all of the meshes used in the results section.

3.3. Numerics

The ANSYS Fluent [35] software package was used to solve the governing equations, and an incompressible, constant density, implicit formulation was chosen for this study. Second order gradient operators were used for the continuity and momentum equations (Eqs. (1)-(2)), and first order gradient operators were used to solve the transport equations for the $\overline{k}$ and $\overline{\epsilon}$ variables that are needed to close the Reynolds stress σ_{ij}. Fluent's standard wall treatment was chosen for use with the realizable k-ϵ turbulence model. Individual cases were run on between 100 and 300 cpus, and converged after a time period of between twenty minutes and an hour and a half.

Flow Plate Design	Electrode Thickness [mm]	Mesh Cells [million]
10 cm^2 serpentine	0.4	10.0 / 11.2
50 cm^2 serpentine	0.4	6.9 / 10.2 / 14.0 / 20.2
50 cm^2 serpentine	1.2	21.0
50 cm^2 serpentine	2.4	23.4
50 cm^2 loose idff	0.4	5.7
50 cm^2 loose idff	1.2	11.5
50 cm^2 loose idff	2.4	24.1
50 cm^2 tight idff	0.4	23.4
50 cm^2 tight idff	1.2	30.9
50 cm^2 tight idff	2.4	26.9
400 cm^2 loose idff	0.4	35.6

Table 2: Sizes of the half cell meshes.

4. Results

Simulation results are presented next. First, pressure drops across the half cells are shown as a function of system parameters. Second, the flux of reactants across the interface between the flow channels and the electrode is analyzed. Third, the flow through several cases is visualized to study electrode transport processes in more detail. Fourth, the existence of flow dead zones that may contribute to the type of degradation seen in Fig. 1 is investigated. Finally, convective and diffusive timescales in the electrode are compared across several plate designs and flow rates.

4.1. Pressure losses

Pressure drops across the half cells are plotted in Fig. 5. Figure 5a shows the pressure drop versus the area specific flow rate, q, for all flow plate designs when they are paired with a 0.4 mm electrode. For reference, linear (i.e. q^1) and quadratic (q^2) scaling relationships are drawn as thin black lines in the top part of the figure. In the limit of pure porous media flow where connective and diffusive transport are neglected, the momentum transport equation (Eq. (2)) reduces to,

$$\frac{\partial}{\partial x_i}\left(\overline{p}\right) = -\frac{\overline{\rho}\nu}{\gamma\kappa}\overline{u}_i, \tag{5}$$

and the pressure drop is expected to scale linearly with the flow rate. In typical channel flow, however, pressure drops scale linearly with flow rate at low Reynolds numbers but quadratically with flow rate at high Reynolds numbers. A scaling power of greater than one can also be expected in flow around channel bends. The interaction of these different relationships produces the complex scaling behavior seen in Fig. 5, where scaling powers vary between one and two as a function of plate design and flow rate. For example, the scaling power of the interdigitated designs tends to increase with the flow rate, reaching nearly quadratic scalings at high flow rates. Conversely, the serpentine designs exhibit a more constant and lower magnitude scaling power. Pressure drops through flow channels are therefore more significant in the interdigitated designs, and pressure drops through electrodes are more significant in the serpentine designs.

Direct relationships between flow plate design and pressure drop can be seen by comparing the cases with active cell areas of 50 cm^2 in Fig. 5a. The serpentine design produces the largest pressure drop, while the loose interdigitated design produces a slightly larger drop than the tight interdigitated design. This behavior is consistent with the data from [24], where serpentine designs led to larger pressure drops than interdigitated designs. At high flow rates, the drops across the interdigitated designs cease to depend on channel spacing. The quadratic scaling behavior and this lack of dependence on channel spacing suggest that high flow rate pressure drops in the interdigitated designs are caused by a combination of the increased friction in the open channel flow and the pressure needed to force fluid through the sharp bends connecting the inlet pipe and the individual open channels.
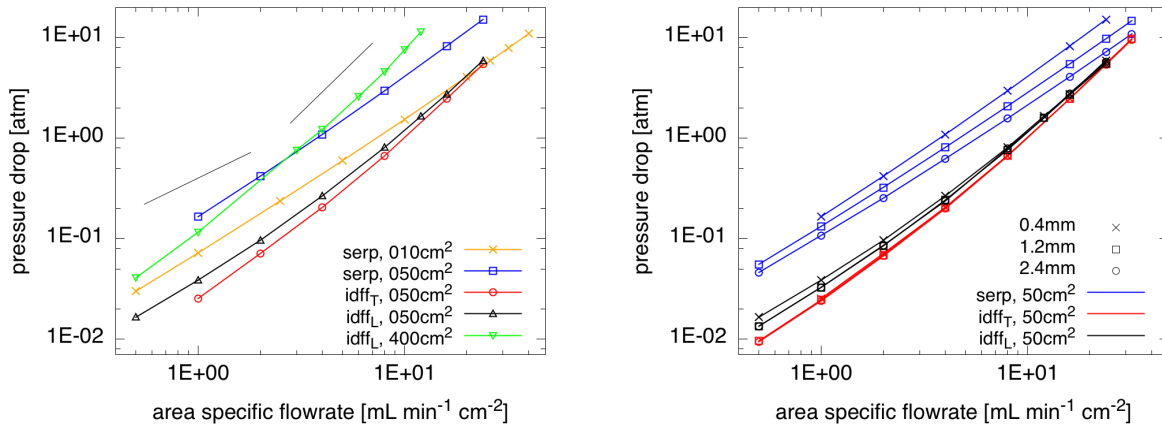
(a) Pressure losses for 0.4 mm electrodes. The thin black lines are linear and quadratic scaling curves.

(b) Pressure loss vs. electrode thickness.
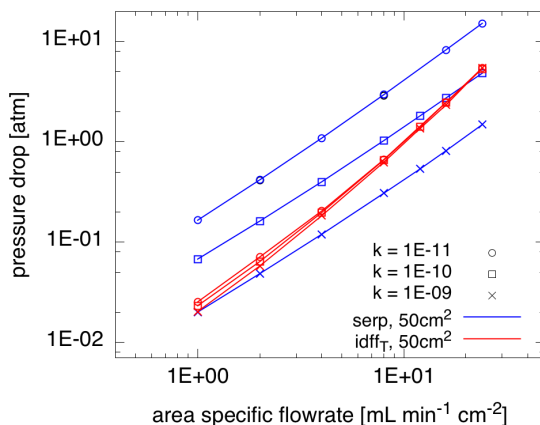
(c) Pressure loss vs. electrode permeability.

Figure 5: Pressure drops across one half of the flow battery system, calculated as a function of active cell area, cell design, electrode thickness, electrode permeability, and flow rate. The 'T' and 'L' subscripts refer to the tight and loose interdigitated flow channel spacings, respectively.

Figure 5b shows how pressure loss is influenced by electrode thickness, and Fig. 5c shows the influence of electrode permeability. These figures use data only from cells with active areas of 50 cm^2. Symbols denote the electrode thickness and permeability in the respective plots, while line colors denote the flow plate designs. The trends from these two figures are similar in that the pressure loss in the serpentine designs is strongly sensitive to the electrode parameters, while the loss in the interdigitated designs is not. This is a further indication that flow through the electrode makes a relatively more important contribution to the serpentine pressure drop than it does to the interdigitated pressure drop.

Figure 5a can also be used to examine how pressure drops scale with cell size. The 400 cm^2 loose interdigitated design exhibits a significantly larger drop than the 50 cm^2 design, even after the flow rate has been normalized by the cell area. As the cell area increases, the mean velocity in an individual interdigitated channel must increase to keep the area specific flow rate constant. These higher channel velocities lead to increases pressure drops. Scaling analyses must carefully account for these non-linear geometric and flow effects when predicting the behavior of industrially relevant 1000 cm^2 cells. Other such effects include the pressure required to move reactants through and out of the large distribution channels (the especially wide channels oriented perpendicular to the bulk flow direction in Fig. 3e) that connect the inlet and outlet pipes to the individual flow channels. Unlike the flow rate, the size of these distribution channels will not be scaled
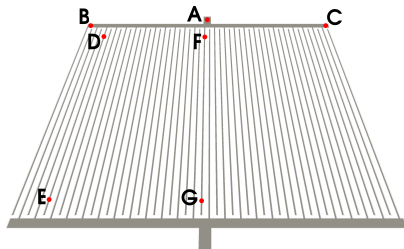
(a) Pressure tap locations.

Flow Pathway	Pressure Drop [atm]	Pressure Drop [% of total]
A → B	1.89	25%
A → C	1.95	26%
A → F	1.88	25%
D → E	0.61	8%
F → G	1.28	17%

(b) Pressure drop magnitudes.

Figure 6: Pressure drops across flow pathways from a plane cut through the open flow channels of the 400 cm^2 loose interdigitated design. The flow rate is 10 mL min^{-1} cm^{-2} and the slice is taken halfway up the open channels. Point A represents the inlet, and the total pressure drop is 7.57 atm.

linearly with the cell area. This creates increasingly large velocities and pressure losses in the main channels at higher flow rates. A simple extrapolation of results obtained for cells with small active areas will not sufficiently capture these effects.

In the first paper [7] of this series, a value of approximately 10 mL min^{-1} cm^2 was discussed as a target area specific flow rate for a high power density flow battery. Additionally, a value of approximately 1 atm was discussed as being a typical maximum allowable pressure drop through an individual cell. Figure 5a indicates that, at a flow rate of 10 mL min^{-1} cm^2, changing the design of a 50 cm^2 cell from a serpentine layout to an interdigitated layout would keep the pressure drop within an acceptable window. In a more industrially relevant 400 cm^2 cell, however, the pressure drop significantly exceeds 1 atm at this target flow rate. This motivates the need for additional engineering that can further limit pressure drops.

Insight into this need for additional engineering can be gained by examining pressure drops across specific flow pathways in the 400 cm^2 cell. These pressure drops are presented in Fig. 6, where data is taken from a single cut plane (Fig. 6a) that is located halfway up the open flow channels. The relative contributions of the pressure drops along given pathways are tabulated in Fig. 6b. For example, the pressure drop between points F and G of the cut plane is 17% of the pressure drop across the entire half cell. This tabulated data demonstrates that at high flow rates a significant fraction of the total pressure head is needed just to move fluid from the main inlet pipe into the open flow channels. Similarly large pressure losses occur as the flow moves from the individual flow channel outlets to the pipe through which all flow exits the half cell. Modifying the geometry of the inlet and outlet pipes, and of the large cross channels that transport reactants to and from individual flow channels, is therefore a realistic option for reducing pressure drops in industrially sized, high power designs.

4.2. Flux pathways

Developing an understanding of how reactants are brought to electrochemically active sites requires understanding fluxes between open flow channels and the porous electrode. These fluxes are fundamentally different in the serpentine and interdigitated designs. In interdigitated designs, half of the channels only transport fresh reactants into the electrode, while the other half only transport products out of the electrode. Conversely, in serpentine designs a single channel might alternate between transporting a reactant mixture into the electrode and out of the electrode.

Fluxes in the serpentine designs are analyzed first. Figure 7 shows planes in the 10 cm^2 and 50 cm^2 serpentine geometries from which data is extracted for analysis. These planes (colored red) are perpendicular to the direction of bulk fluid flow. They are separated into two regions: one consisting of material within the open flow channels, and the other consisting of material within the electrode. The normal flux through each of these areas is computed, and the results describe how much of the total flow passes through the open channels and how much passes through the electrode. Note that the planes cut across the channel bends, rather than through the long channel sections. This choice was made so that the open channel flow would be moving normal to the analysis plane.

Fluxes through the cut planes in Fig. 7 are plotted in Fig. 8 as a function of the area specific flow rate. Fluxes from the 50 cm^2 design are calculated for all three electrode thicknesses, while 10 cm^2 results are

9
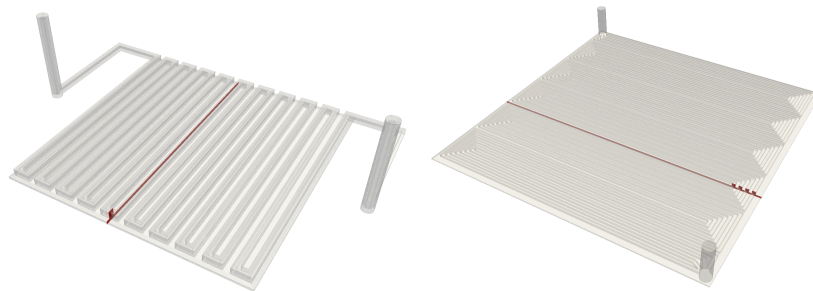
(a) 10 cm², serpentine, single channel. (b) 50 cm², serpentine, four channels.

Figure 7: Planes in the serpentine flow plates which are used to determine the split between flux through the open channels and flux through the electrode.
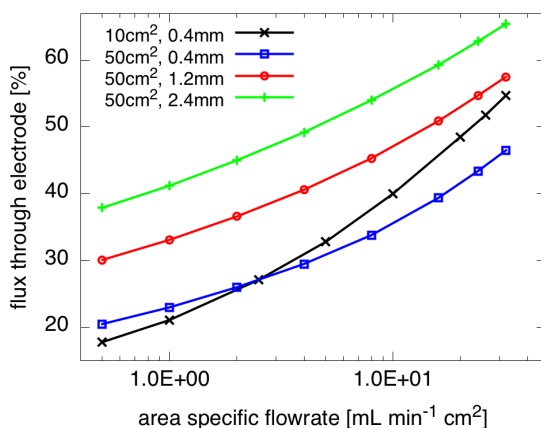
Figure 8: Percentage of the total normal flux that passes through the electrode in the serpentine flow plate cut planes shown in Fig. 7. The remainder of the normal flux passes through the open flow channels.

shown only for a 0.4 mm electrode. The Fig. 8 data shows the percentage of the total flux that passes through the electrode, with the remainder of the flux passing through the open channels. The split of the flow between these two pathways depends strongly on the flow rate, and varies from 20% through the electrode to 60% through the electrode. As the flow rate increases, more flow goes through the electrode. A physical mechanism contributing to this behavior is the scaling relationship between pressure and flow rate. As flow rates increase, pressure drops in the open channels will begin to scale quadratically with flow rate, while pressure drops in the electrode will continue to scale linearly. The relative resistance of the electrode therefore tends to decrease as the flow rate increases. This forces an increasing percentage of the reactant stream through the electrode. This observation might be particularly utilized in a flow battery's control system, for example by periodically flushing used reactants from the system with short flow rate pulses.

A different flux analysis is performed for the interdigitated designs, where all of the fluid must pass through the electrode. As shown in Fig. 9, vectors are drawn along the electrode / flow channel interface in each of the three interdigitated designs. The vectors run most of the length of the flow channels. Velocities are extracted along these vectors and plotted in Fig. 10 to understand the flux between the open channels and the electrode. Two components of the velocity field are interrogated. The first is aligned with the channel, and the second points from the channel into the electrode (normal to the channel and electrode interface). This second component characterizes the flux out of the channel and into the electrode. Velocities are plotted for three different flow rates for each of the three interdigitated designs.

The important information that Fig. 10 reveals is the difference between the speed at which reactants move along a channel and the speed at which reactants move out of a channel. This difference is simply the gap between the dashed and solid lines describing a given case. In the loosely spaced 50 cm² design, these

10

(a) 50 cm² loose interdigitated   (b) 50 cm² tight interdigitated   (c) 400 cm² loose interdigitated
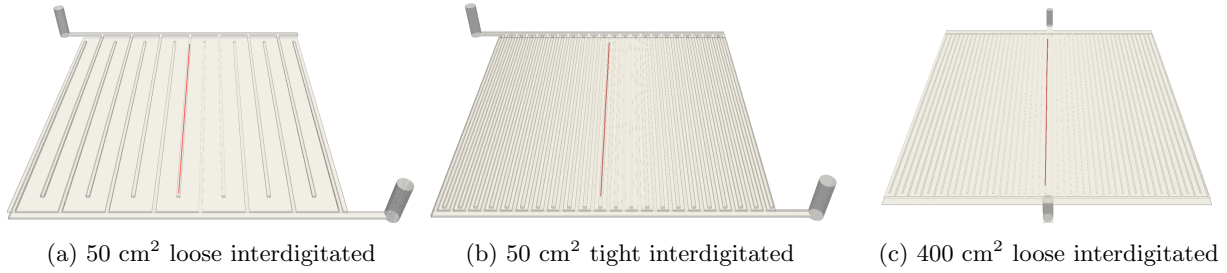
Figure 9: Vectors in the interdigitated flow plates along which velocity profiles are extracted for analysis. These vectors exist within the plane where the electrode meets the open flow channels.

(a) 50 cm² loose interdigitated

(b) 50 cm² tight interdigitated

(c) 400 cm² loose interdigitated
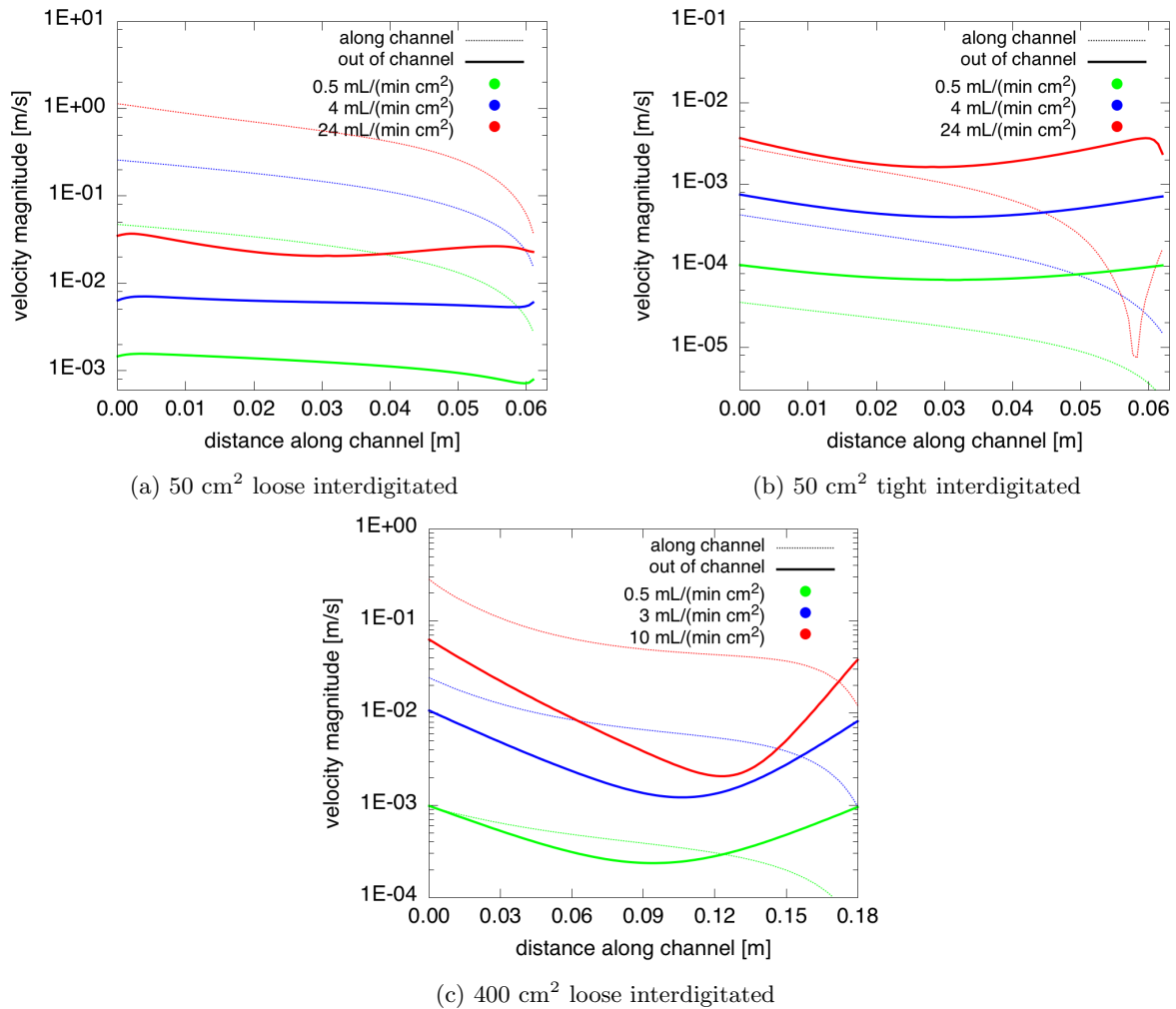
Figure 10: Interdigitated flow plate velocity profiles extracted from the interdigitated flow plate vectors shown in in Fig. 9.

gaps are large. Flow moves relatively quickly along each channel and relatively slowly out of the channels. The gaps occur because the loosely spaced design uses only a few channels to carry the entire reactant supply. Consequently, the channel aligned velocities must be high. It might be expected that the flux out of the channels would also be high, and indeed these fluxes have a higher magnitude than the corresponding fluxes in the tightly spaced 50 cm² design. But, Fig. 10 reveals this effect to be nonlinear. Channel aligned

11
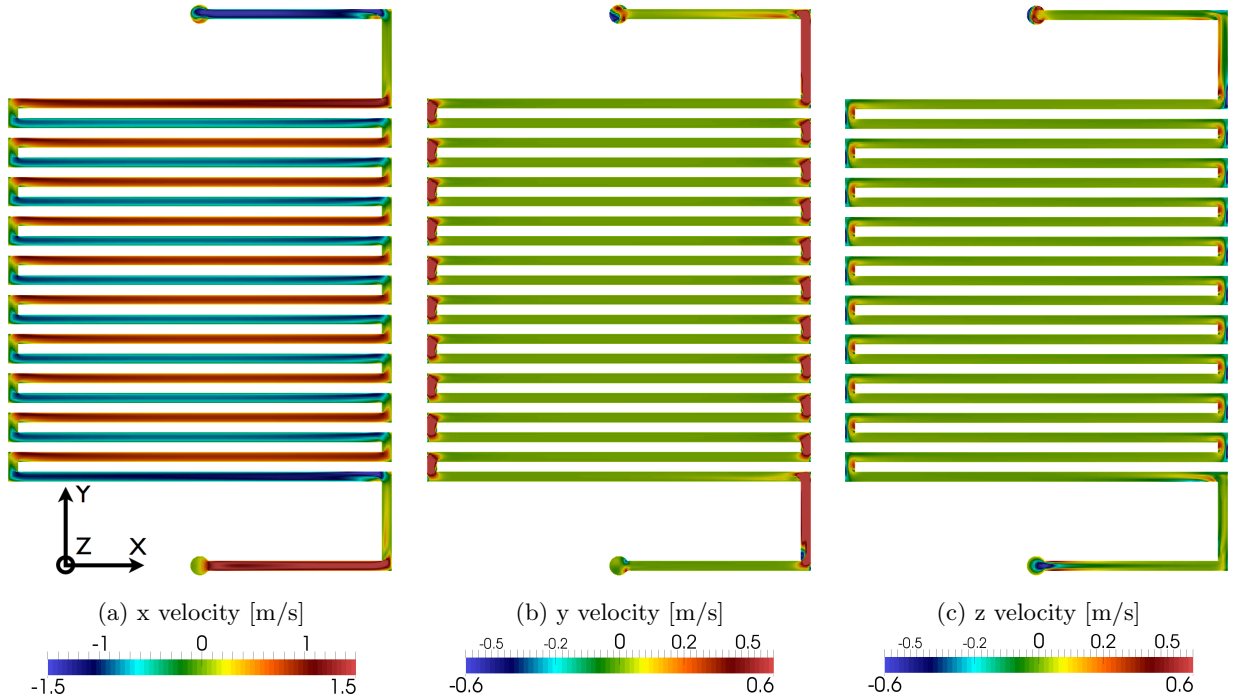
Figure 11: Velocity contour plots from a plane cut halfway (0.4 mm) through the depth of the flow channels of the 10 cm^2 single channel serpentine flow plate with a 0.4 mm electrode and a flow rate of 5 mL min^{-1} cm^{-2}.

velocities increase faster than out-of-channel velocities as the channel spacing is increased.

The 400 cm^2 loose interdigitated results in Fig. 10c are qualitatively similarity to the 50 cm^2 results, with one exception. As the end of the channel is approached, the out-of-channel velocity rises dramatically. This effect is of course caused by pressure resistance from the channel endwall that forces reactants into the electrode. The noteworthy result from Fig. 10c is how the endwall effect penetrates much farther upstream in a cell with a larger active area. This effect may contribute to the nonlinear growth of the pressure drop with cell size that was discussed in section 4.1.

4.3. Flow visualization

Several half cell flow fields are visualized to provide additional insight into how transport processes depend on flow plate design. Velocity fields from the 10 cm^2 serpentine design are shown first, in Figs. 11 and 12. Figure 11 shows contour plots of all three velocity components on a plane halfway up the height of the flow channels. Figure 12 shows the corresponding plots from a plane halfway up the height of the electrode.

The velocity contours in Fig. 11 indicate standard channel flow, with some added vortical effects visible around channel bends in the out-of-plane velocities (Fig. 11c). Velocity fluxes into the electrode are not distinguishable at these contour ranges and in a plane that is relatively far from the electrode interface. Figure 12, however, does reveal interesting features of transport within the electrode. In-plane flow largely follows the channel paths, as seen in the oscillating pattern of positive and negative velocity regions in Fig. 12a. Figure 12c shows the movement of reactants into and out of the electrode. Reactants tend to be pushed into the electrode (blue coloring in Fig. 12c) below the 'downstream' half of flow channel bends, and to be pushed back into the channels (red coloring) below the 'upstream' half of flow channel bends. This behavior is driven by the pressure differential between adjacent open channels. As flow approaches the upstream half of a channel bend, the path of least pressure resistance is to continue in the open channel around the bend. After fluid rounds the bend, however, it can only reach the adjacent bend through an open channel by twice traversing the entire width of the flow plate. An alternative flow path is to move only a single channel width through the electrode, and into the next bend. Although this alternative path crosses porous media, the path length is very short compared to the open channel path. Flow therefore

(a) x velocity [m/s]

(b) y velocity [m/s]

(c) z velocity [m/s]
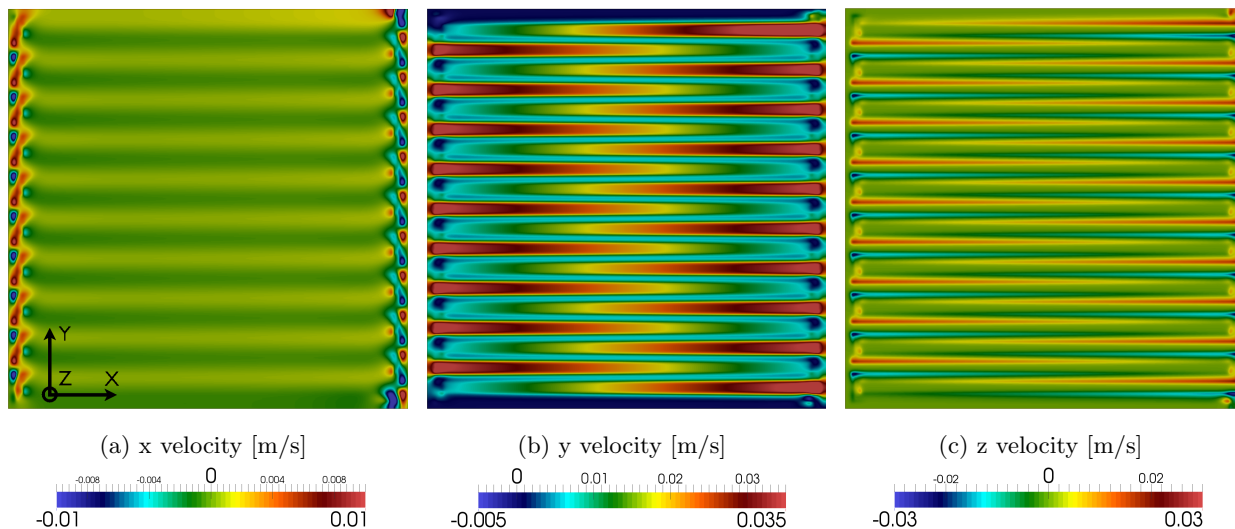
Figure 12: Velocity contour plots from a plane cut halfway (0.2 mm) through the depth of a 0.4 mm electrode attached to a 10 cm^2 single channel serpentine flow plate, for a flow rate of 5 mL min^{-1} cm^{-2}.

tends to push into the electrode in the downstream half of the channel bends, and to rise back into open channels in the upstream half of the channel bends. As reactants traverse the width of the plate through the long channels, some flux across the channel and electrode interface continues, but the strength of this flux diminishes with distance from the bends.

Velocity contours from the 400 cm^2 interdigitated flow plate are shown in Figs. 13 and 14. Large scale asymmetries are observed in the open channels in Fig. 13, with flow traveling most quickly through the channels at the center of the plate. This indicates significant pressure resistance from the flow through the horizontal (x direction) distribution channel. Additionally, channel aligned velocities vary significantly between the beginning of each channel and the end. These variations are consistent with the interface velocity curves in Fig. 10c. Velocities in the electrode are again more interesting because they highlight how reactant transport occurs. The cross-channel velocity component in Fig. 14a demonstrates the bifurcation of the paths of reactants that are pushed into the electrode. Reactants that are pushed in from the right half of a channel will be convected toward the nearest channel to the right, and reactants pushed in from the left half of a channel will be convected toward the left. A comparison of Figs. 14a and 14b additionally demonstrates that this cross channel convection is much stronger than convection in the channel aligned direction.

Flow is also visualized on a set of planes that simultaneously cut through the open channels and the electrode. The locations of these planes are shown in Fig. 15, with the three planes from the 50 cm^2 cell appearing in Fig. 15a, and the three planes from the 400 cm^2 cell appearing in Fig. 15b. Velocity contours from the first of these plane sets are shown in Fig. 16. The contour range in the channel aligned plots (Figs. 16a - 16c) is set to reveal electrode flow, so that contours of the relatively fast flow through the open channels saturate the color spectrum. The fast open channel flow drives flow in the channel aligned (y) direction in the electrode, at locations just below the porous media interface. These channel aligned electrode velocities peak around 0.06 m/s in the immediate vicinity of the interface, but for the most part their magnitudes are much smaller. These magnitudes can be compared to the the cross-channel (x) velocities in Figs. 16g - 16i to understand how flow behaves as a function of electrode depth. While flow is pulled in the channel aligned direction near the interface, it quickly transitions to moving laterally toward adjacent open channels as it penetrates deeper into the electrode. Note, however, that these velocity magnitudes depend on the extent to which reactants have progressed between the cell inlet and outlet. For example, velocities near the middle of the cell (Figs. 16e and 16h) are smaller in magnitude than those near the inlet or outlet.

A similar set of velocity contours from a 50 cm^2 tight interdigitated cell simulation are visualized to understand the influence of channel spacing in Fig. 17. There, the channel aligned (Figs. 17a - 17c) contour range has been adjusted to highlight flow structures within the open channels. A comparison of Fig. 17a
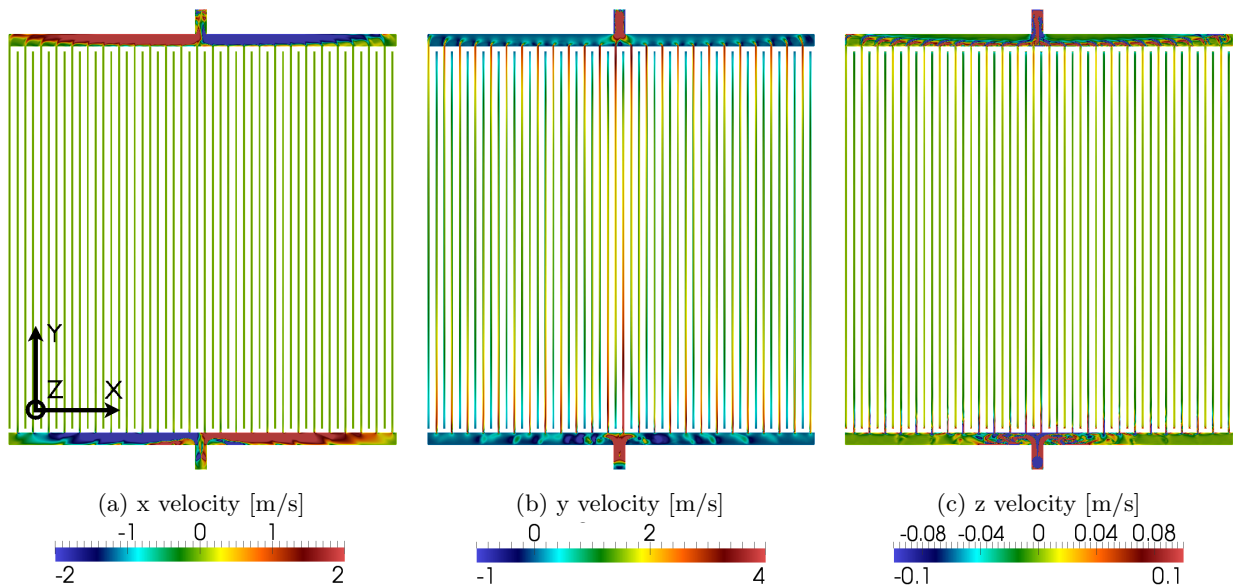
Figure 13: Velocity contour plots from a plane cut halfway (0.4 mm) through the depth of the flow channels of the 400 cm^2 loose interdigitated flow plate with a 0.4 mm electrode and a flow rate of 6 mL min^{-1} cm^{-2}.
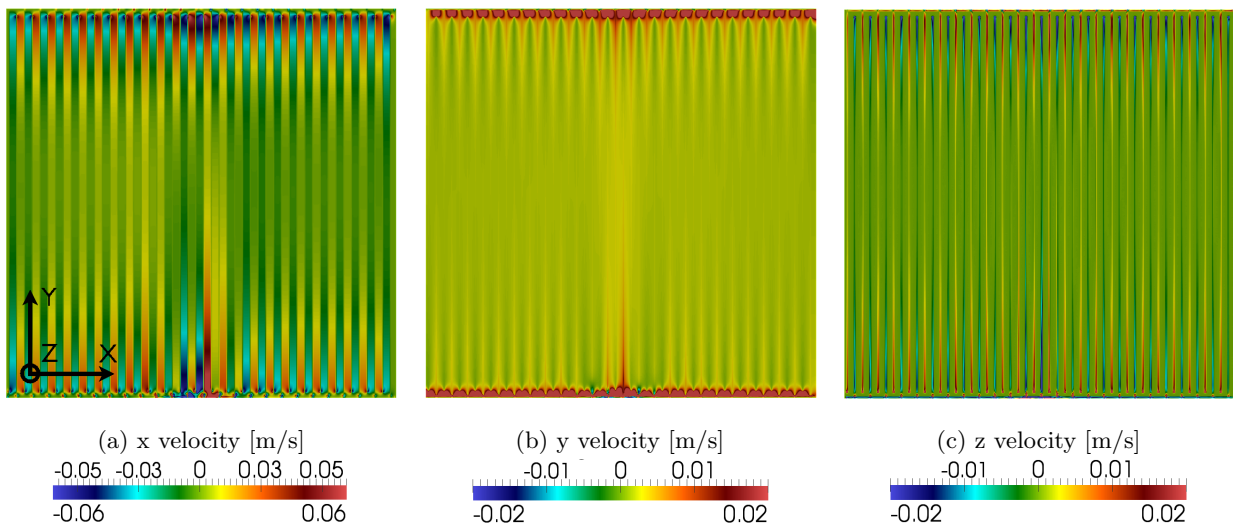
Figure 14: Velocity contour plots from a plane cut halfway (0.2 mm) through the depth of a 0.4 mm electrode attached to a 400 cm^2 loose interdigitated flow plate, for a flow rate of 6 mL min^{-1} cm^{-2}.

and Fig. 17c particularly demonstrates how flow transitions from being fast in the inlet channels on one side of the half cell to being fast in the outlet channels on the other side of the half cell. Some quantitative differences are seen when comparing in-plane velocities in Figs. 17d - 17i with the corresponding velocities in the 400 cm^2 cell. For example, the cross channel (x) velocities in Figs. 16a - 16c exhibited alternating positive and negative bands in regions between channels. In Figs. 17d - 17i, the cross channel velocities alternate between larger positive and smaller positive values. This bias toward positive values occurs because the inlet and the outlet of the 50 cm^2 design are located on opposite sides of the cell. Consequently, reactants must, on average, flow in the positive cross channel direction. In spite of these differences, many of the 50 cm^2 flow structures are qualitatively similar to those seen in Fig. 16. For example, reactants tend to move laterally toward an adjacent open channel after being pushed into the electrode. Designs with a tight channel spacing are characterized by an increased number of channels and a shorter lateral distance between

14

(a) 50 cm^2 tight interdigitated   (b) 400 cm^2 loose interdigitated
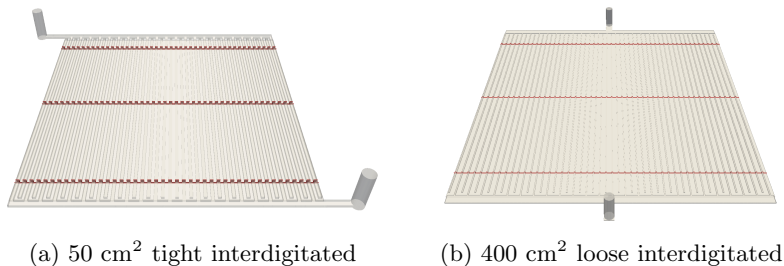
Figure 15: Locations of the cut planes that are used in Figs. 16 and 17 for flow visualization.

channels. Consequently, in these designs reactants flow at a somewhat slower speed through a shorter path to reach adjacent open channels. These effects help reduce the magnitude of the tight 50 cm^2 design's pressure drop, relative to the drop in the loose 50 cm^2 design.

4.4. Dead zones

Developing a full understanding of the degradation processes shown in Fig. 1 requires the modeling of scalar transport and electrochemical behavior in addition to flow transport. Nevertheless, flow modeling can provide insight into degradation drivers. Figure 18 shows velocity magnitude contours from a cut plane through a simulation of the 50 cm^2 serpentine design. The flow rate in this simulation was set as 2 mL min^{-1} cm^{-2} (100 mL min^{-1}) to match the conditions of the experiment highlighted in Fig. 1. The visualized cut plane is located 0.3 mm below the electrode / flow channel interface, or 75% through the depth of the electrode.

The velocity contours in Fig. 18 depict a pattern of particularly low speed flow in electrode regions underneath bends in the serpentine flow field. Between these low speed regions, thin regions of particularly high speed flow are found where reactants move through the electrode as alternative means of reaching the next bend. This preferential movement through the electrode occurs because the path through the open channels traverses the full width of the cell twice, generating a significant pressure drop.

A comparison of Fig. 18 and Fig. 1 indicates significant correlation between regions where degradation is experimentally observed and regions where flow through the electrode is particularly slow. These regions are found in the immediate vicinity of the flow channel bends. Such correlation cannot be used to fully explain the observed degradation, but it is consistent with the idea that insufficient reactant transport to electrochemically active sites can drive degradation.

4.5. Timescale analysis

Flow battery flow field designs should ideally ensure that velocities are reasonably large throughout the battery electrode. If low velocity regions do form, only diffusion and migration can transport reactants to electrochemically active sites. Diffusion and migration may be significantly slower than convection, however, and they may not be able to provide a sufficient supply of reactants to the active sites. Insufficient reactants lead to increasing cell voltages, and possibly to the kind of corrosive damage seen in Fig. 1.

Ensuring sufficient convection throughout an electrode is difficult because it requires an understanding of both localized electrochemical behavior and localized flow behavior. A qualitative understanding of sufficient convection can be developed, however, by considering time scales within the electrode. These timescales help to expose the relative importance of diffusion and convection as a function of electrode thickness, cell size, and flow rate.

Convective and diffusive timescales are defined as

$$t_c = \frac{L}{u_{n,b}}, \tag{6}$$

$$t_d = \frac{L^2}{D_r}, \tag{7}$$

where $L = 5\text{E-}5$ m is a characteristic length scale which is assumed to be $1/8^{th}$ of the 0.4 mm electrode thickness, $D_r = 1\text{E-}9$ m^2/s is a characteristic liquid phase diffusivity (e.g., for Br$_2$ in water), and $u_{n,b}$ is

15
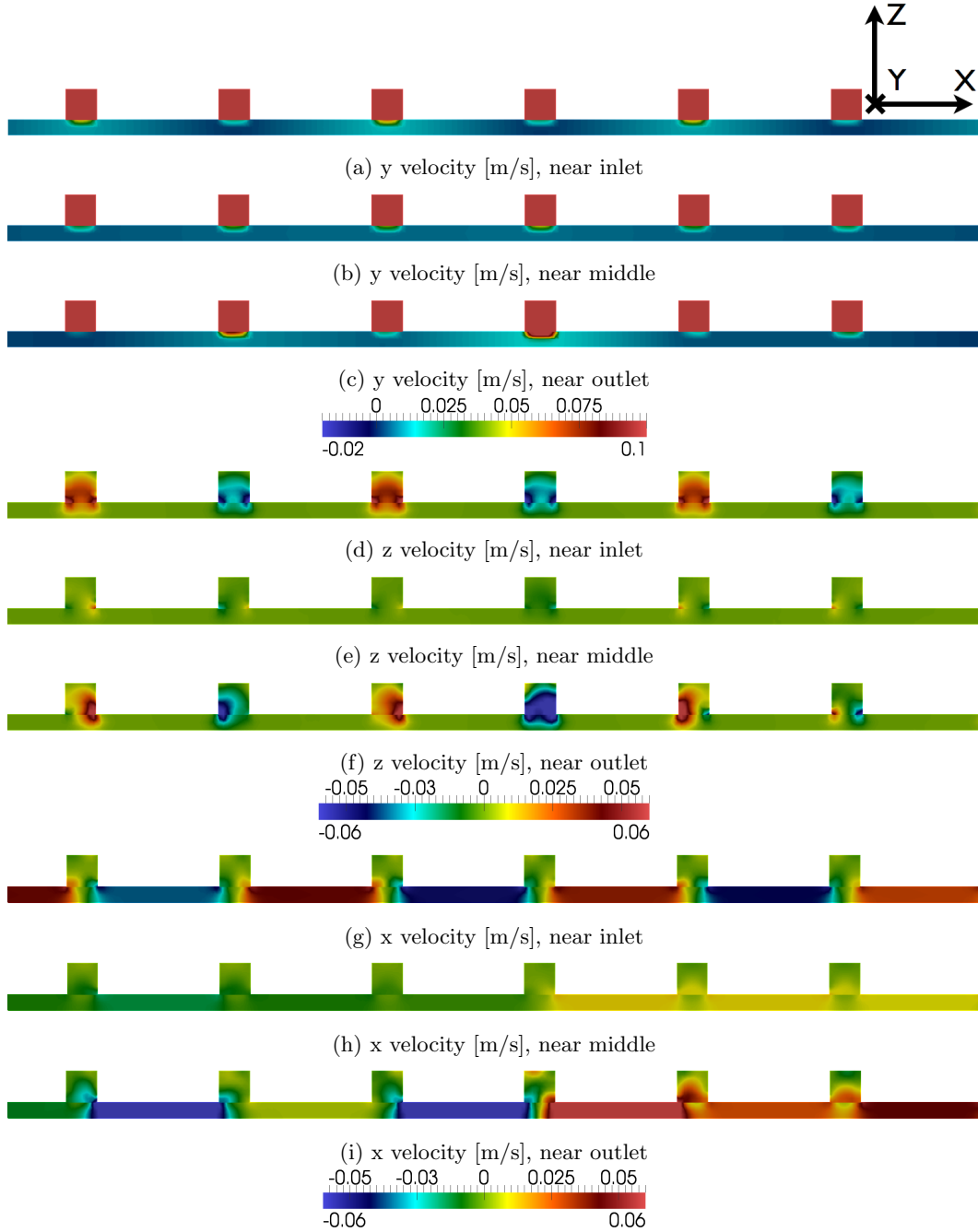
Figure 16: Velocity contours from the $400 \, \text{cm}^2$ loose interdigitated design for a flow rate of $10 \, \text{mL} \, \text{min}^{-1} \, \text{cm}^{-2}$. The locations of the cut planes are shown in Fig. 15b.

a velocity from the data extraction planes in Fig. 7. This velocity is calculated by averaging the velocity component pointing normal to the extraction planes over the electrode area. Physically, $u_{n,b}$ represents the bulk velocity passing through the electrode between the flow plate's inlet and outlet.

Timescales formulated using these quantities are shown in Fig. 19 for both the $10 \, \text{cm}^2$ and $50 \, \text{cm}^2$ serpentine designs, and for several flow rates and electrode thicknesses. The diffusive timescale is always at least two orders of magnitude larger than the convective timescale, highlighting the extent to which convection is relied upon for reactant transport. Design parameters are responsible for only half of an order
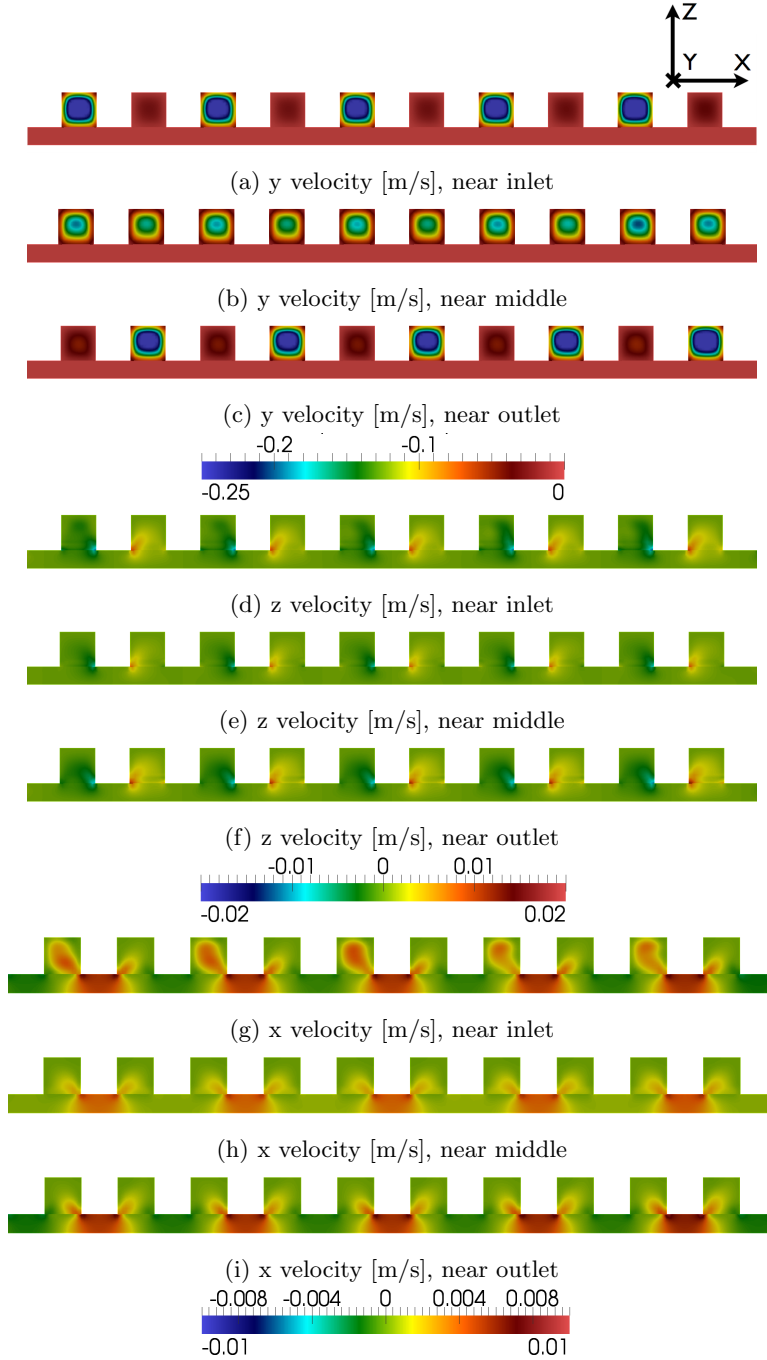
Figure 17: Velocity contours from the 50 cm^2 tight interdigitated design for a flow rate of 8 mL min^{-1} cm^{-2}. The locations of the cut planes are shown in Fig. 15a.

of magnitude change in convective timescales for a given flow rate. The bulk convection timescale, however, neglects the effects of local low velocity regions in the electrode. If the velocity in such a region is one or two orders of magnitude smaller than the bulk velocity, reactant transport will likely be insufficient and cell performance will suffer. Determining the exact timescale at which these effects take place requires a fully coupled flow and electrochemistry solver.

(a) velocity magnitude [m/s]
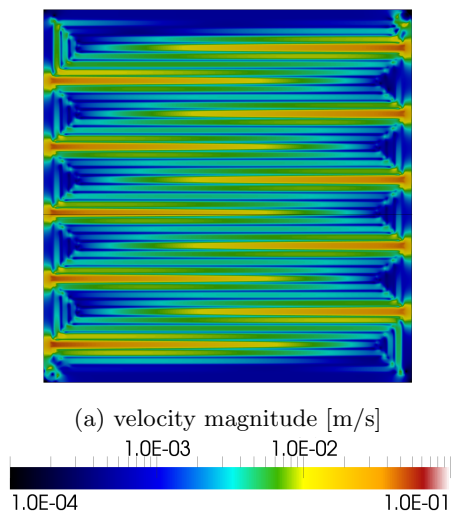
Figure 18: Velocity magnitudes in a cut plane located 0.3 mm (75% of the electrode thickness) below the flow channel / electrode interface, taken from a 50 cm^2 serpentine, 0.4 mm electrode case. The flow rate is set as 2 mL min^{-1} cm^{-2} to approximately match the flow rate from the experiment shown in Fig. 1.
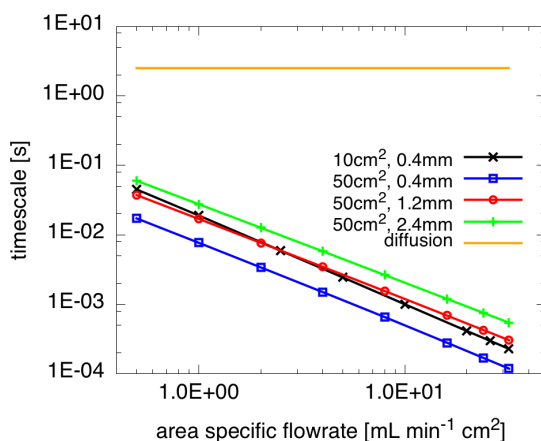
Figure 19: Convective timescales in the serpentine flow plate designs, computed using the bulk velocity of the flow through the electrode in the cut planes shown in Fig. 7.

5. Conclusions

A computational flow solver has been used to describe the hydrodynamics of a variety of flow battery half cell designs. Results have demonstrated that high-resolution CFD studies can provide detailed insight into flow patterns, and quantify properties of interest such as pressure drops, flow uniformity, and the presence of flow dead zones. It was shown that for a given flow rate and cell size, switching from a serpentine to an interdigitated design significantly reduces the pressure drop, and that interdigitated designs are promising for flow batteries with high power densities. Quantitative simulation results, however, revealed that adequate pressure drops for industrially practical cell sizes of 1000 cm^2 require optimization beyond the simple designs considered here. This design optimization could be readily performed without adjusting the modeling platform.

The mechanisms that affect pressure drops in interdigitated and serpentine flow field designs were particularly studied. These mechanisms included how pressure gradients scale with velocity in different flow environments, and how reactants are transported through the porous electrode and back into open flow channels. Tighter interdigitated channels were shown to offer slightly lower pressure drops than loosely spaced

18

channels, and pressure drops were shown to scale non-linearly with the active cell area. Finally, analysis showed that, for high-power flow batteries, diffusion time scales are 2-3 orders of magnitude slower than convective time scales. This emphasizes the importance of flow engineering to high-power designs.

Acknowledgements

[1] C. Ponce de León, A. Frías-Ferrer, J. González-García, D. A. Szánto, and F. C. Walsh. Redox flow cells for energy conversion. *J. of Power Sources*, 160(1):716–732, 2006.

[2] H. Chen, T. N. Cong, W. Yang, C. Tan, Y. Li, and Y. Ding. Progress in electrical energy storage system: A critical review. *Prog. Natural Science*, 19(3):291–312, 2009.

[3] A. Z. Weber, M. M. Mench J. P. Meyers, P. N. Ross, J. T. Gostick, and Q. Liu. Redox flow batteries: a review. *J. Applied Electrochemistry*, 41(10):1137–1164, 2011.

[4] A. Ipakchi and F. Albuyeh. Grid of the future. *IEEE Power and Energy Magazine*, 7(2):52–62, 2009.

[5] B. Dunn, H. Kamath, and J. M. Tarascon. Electrical energy storage for the grid: A battery of choices. *Science*, 334(6058):928–935, 2011.

[6] K. T. Cho, P. Ridgway, A. Z. Weber, S. Haussener, V. Battaglia, and V. Srinivasan. High performance hydrogen/bromine redox flow battery for grid-scale energy storage. *J. Electrochem. Soc.*, 159(11):A1806–A1815, 2012.

[7] P. Albertus, E. Knudsen, and A. Kojic. High power flow batteries i: Design requirements. *J. Electrochem. Soc.*, (Submitted), 2014.

[8] K. T. Cho, P. Albertus, V. Battaglia, A. Kojic, V. Srinivasan, and A. Z. Weber. Optimization and analysis of high-power hydrogen/bromine-flow batteries for grid-scale energy storage. *Energy Technology*, 1(10):596–608, 2013.

[9] N. Pekula, K. Heller, P. A. Chuang, A. Turhan, M. M. Mench, J. S. Brenizer, and K. Ünlü. Study of water distribution and transport in a polymer electrolyte fuel cell using neutron imaging. *Nuclear Instruments & Methods In Physics Research A*, 542(1-3):134–141, 2005.

[10] S. Um, C. Y. Wang, and K. S. Chen. Computational fluid dynamics modeling of proton exchange fuel cells. *J. Electrochem. Soc.*, 147(12):4485–4493, 2000.

[11] T. Berning and N. Djilali. A 3D multiphase, multicomponent model of the cathode and anode of a PEM fuel cell. *J. Electrochem. Soc.*, 150(12):A1589–A1598, 2003.

[12] K. W. Lum and J. J. McGuirk. 2D and 3D modeling of a PEMFC cathode with interdigitated gas distributors. *J. Electrochem. Soc.*, 152(4):A811–A817, 2005.

[13] D. H. Schwarz and N. Djilali. 3D modeling of catalyst layers in PEM fuel cells. *J. Electrochem. Soc.*, 154(11):B1167–B1178, 2007.

[14] E. U. Ubong, Z. Shi, and X. Wang. Three-dimensional modeling and experimental study of a high temperature PBI-based PEM fuel cell. *J. Electrochem. Soc.*, 156(10):B1276–B1282, 2009.

[15] R. M. Darling and P. Badrinarayanan. Oxygen transport in polymer-electrolyte fuel cells with interdigitated air channels in porous bipolar plates. *J. Electrochmical Soc.*, 158(1):B54–B60, 2011.

[16] W.-M. Yan, H.-Y. Li, and W.-C. Tsai. Three-dimensional analysis of PEMFCs with different flow channel designs. *J. Electrochem. Soc.*, 153(10):A1984–A1991, 2006.

[17] C.-H. Huang and J.-W. Lin. Optimal gas channel shape design for a serpentine PEMFC: theoretical and experimental studies. *J. Electrochem. Soc.*, 156(1):B178–B187, 2009.

[18] P. K. Sinha, C.-Y. Wang, and U. Beuscher. Transport phenomena in elevated temperature PEM fuel cells. *J. Electrochem. Soc.*, 154(1):B106–B116, 2007.

[19] M. Kvesić, U. Reimer, D. Froning, L. Lüke, W. Lehnert, and D. Stolten. 3D modeling of a 200 cm^2 HT-PEFC short stack. *Int. J. Hydrogen Energy*, 37(3):2430–2439, 2012.

[20] F. Liu, M. Kvesic, K. Wippermann, U. Reimer, and W. Lehnert. Effect of spiral flow field design on performance and durability of HT-PEFCs. *J. Electrochem. Soc.*, 160(8):F892–F897, 2013.

[21] A. P. Manso, F. F. Marzo, J. Barranco, X. Garikano, and M. Garmendia Mujika. Influence of geometric parameters of the flow fields on the performance of a PEM fuel cell. A review. *Int. J. Hydrogen Energy*, 37(20):15256–15287, 2012.

[22] M. Rychcik and M. Skyllas-Kazacos. Characteristics of a new all-vanadium redox flow battery. *J. Power Sources*, 22(1):59–67, 1995.

[23] R. S. Yeo and D. T. Chin. A Hydrogen-Bromine cell for energy storage applications. *J. Electrochem. Soc.*, 127(3):549–555, 1980.

[24] T. Jyothi Latha and S. Jayanti. Hydrodynamic analysis of flow fields for redox flow battery applications. *J. Appl. Electrochem*, 44(9):995–1006, 2014.

[25] V. E. Brunini, Y.-M. Chiang, and W. C. Carter. Modeling the hydrodynamic and electrochemical efficiency of semi-solid flow batteries. *Electrochemica Acta*, 69:301–307, 2012.

[26] M. Duduta, B. Ho, V. C. Wood, P Limthongkul, V. E. Brunini, W. C. Carter, and Y. Chiang. Semi-solid lithium rechargeable flow battery. *Adv. Energy Materials*, 1(4):511–516, 2011.

[27] K. C. Smith, Y.-M. Chiang, and W. C. Carter. Maximizing energetic efficiency in flow batteries utilizing non-newtonian fluids. *J. Electrochem. Soc.*, 161(4):A486–A496, 2014.

[28] Nuvera Fuel Cells. Consolidated fuel cell electrode. US Patent Application Publication, Feb. 2010. Pub. No. US 2010/0040926A1.

[29] R. M. Darling and M. L. Perry. The influence of electrode and channel configurations on flow battery performance. *J. Electrochmical Soc.*, 161(9):A1381–A1387, 2014.

[30] J. T. Gostick, M. W. Fowler, M. D. Pritzker, M. A. Ioannidis, and L. M. Behra. In-plane and through-plane gas permeability of carbon fiber electrode backing layers. *J. Power Sources*, 162(1):228–238, 2006.

[31] T.-H. Shih, W. W. Liou, A. Shabbir, Z. Yang, and J. Zhu. A new k-ϵ eddy viscosity model for high reynolds number turbulent flows. *Computers & Fluids*, 24(3):227–238, 1995.

[32] B. E. Launder and D. B. Spalding. The numerical computation of turbulent flows. *Computer Methods in Applied Mechanics and Engineering*, 3(2):269–289, 1974.

[33] W. P. Jones and B. E. Launder. The prediction of laminarization with a two-equation model of turbulence. *Int. J. Heat Mass Transfer*, 15(2):301–314, 1972.

[34] OpenFOAM: An open source C++ computer program. Available from www.openfoam.org.

[35] Fluent. FLUENT software, Release 12.0. Available from ANSYS Inc., Canonsburg, PA, 2011.